Comparisons between Hybrid-PIC Simulation and Plume Plasma Measurements of LaB_6 Hollow Cathode

IEPC-2019-865

Presented at the 36th International Electric Propulsion Conference
University of Vienna, Austria
September 15-20, 2019

K. Kubota*
Japan Aerospace Exploration Agency, Chofu, Tokyo, 182-8522, Japan

Y. Oshio†
Ryukoku University, Otsu, Shiga, 520-2194, Japan

K. Torii‡ and Y. Okuno§
Tokyo Institute of Technology, Yokohama, Kanagawa, 226-8503, Japan

H. Watanabe¶
Tokyo Metropolitan University, Hino, Tokyo, 191-0065, Japan

and

S. Cho‖ and I. Funaki**
Japan Aerospace Exploration Agency, Sagamihara, Kanagawa, 252-5210, Japan

Abstract: The plasma flow of a LaB_6 hollow cathode was simulated using hybrid-PIC (Particle In Cell) model, and was compared with the experimental data measured along the center axis with a Langmuir probe. As an anomalous resistivity model, IAT (Ion Acoustic Turbulence) growth model was used not to overestimate the anomalous effect. In the numerical model, the induced magnetic field in the azimuthal direction was newly implemented, and its effects on the plume characteristics were examined. The results indicate that the accuracy of the axial profiles of the plasma properties in the plume region was improved by including the induced magnetic field. With the magnetic field, the electron number density is increased along the center axis due to the pinch effect caused by Lorentz force. Consequently, the electron temperature is decreased by including the magnetic field and approaches the experimental data. However, the present model is inadequate to capture the radial profile especially of the electron number density in the plume region, hence further investigation is needed in the future.

*Researcher, Aeronautical Technology Directorate, kubota.kenichi@jaxa.jp
†Assistant Professor, Faculty of Science and Technology, oshio@rins.ryukoku.ac.jp
‡Gradiate Student, Department of Mechanical Engineering, torii.k.ad@m.titech.ac.jp
§Professor, Department of Mechanical Engineering, okuno.y.aa@m.titech.ac.jp
¶Assistant Professor, Faculty of System Design, hwatanabe@tmu.ac.jp
‖Researcher, Research and Development Directorate, choh.shinatora@jaxa.jp
**Professor, Institute of Space and Astronautical Science, funaki.ikkoh@jaxa.jp

Nomenclature

B	= magnetic flux density
b	= directional unit vector of magnetic flux density
E	= electric field
e	= elementary charge
j	= current density
k	= Boltzmann constant
m	= mass of particle
n	= number density
p	= pressure
r	= radial coordinate
T	= temperature
u	= velocity of fluid
v	= velocity of particle
W	= wave energy density
z	= axial coordinate
β	= Hall parameter
θ	= azimuthal angle
μ	= mobility
ν	= collision frequency
ϕ	= electric potential
ω	= angular frequency
Subscripts	
e	= electrons
em	= emitter
h	= heavy particles
i	= ions
iz	= ionization
IAT	= ion acoustic turbulence
n	= neutrals
p	= plasma

I. Introduction

For the main propulsion system of all-electric satellite or deep space explorer, R&Ds of high-power Hall thrusters are energetically being carried out in many organizations.[1–7] In Japan, the capabilities of both TAL and SPT type Hall thrusters in that power range are explored to expand the range of options in the future. JAXA, IA, IHI, and Tokyo Metropolitan University have focused on the development of SPT type Hall thruster in the 2-6 kW power range due to its possibilities of broad utility.[8] Since one of the most critical issues is the development of hollow cathode because of its indispensability and sensitivity against impurities, discharge characteristics and dependency on operation conditions of hollow cathodes should be clarified in detail.

In JAXA, a numerical code using hybrid-PIC (Particle In Cell) model has been developed to understand the detailed physics of hollow cathodes, in which heavy particles (neutrals and ions) and electrons are modeled by particles and fluid, respectively. In recent work, the IAT (ion acoustic turbulence) growth model was implemented to capture the transitional growth of anomalous resistivity of electrons.[9,10] In this study, the numerical model was updated so that the self-induced magnetic field in the azimuthal direction could be considered because its non-negligible influences on the plasma properties were reported by JPL.[11] We also measured the plasma characteristics in the plume region using Langmuir probe. In this paper, the numerical results are compared with experimental data of the probe diagnosis in order to validate the simulated results.

II. Plume Plasma Measurements

A. Hollow Cathode

To obtain experimental data to validate simulation, we developed a laboratory model of hollow cathode. Different from conventional hollow cathodes, a radiative heater made of graphite was used to prevent serious failures of a heater caused by thermal stress.[12] The heater was surrounded by a multi-layer Ta foil, and these are contained in a keeper electrode made of graphite. The hollow cathode used LaB_6 as an emitter material because of its robustness against poisoning by oxidizing impurities.[13] The emitter was contained inside a graphite cathode tube which is non-reactive to LaB_6 in a high-temperature environment.

B. Facility and Configuration

The cathode was tested in the vacuum chamber which has a diameter of 0.6 m and a length of 1.0 m. Two vacuum pumps with 4,300 l/sec xenon pumping speed are mounted on this chamber. Without gas injection, the vacuum degree reaches about 10^{-5} Pa. The test was conducted in a diode configuration, that is, the main discharge was maintained between the cathode and a cylindrical anode placed at 20 mm apart from the cathode end as shown in Fig. 1.

The plume plasma properties were measured by the Langmuir probe mounted on a two-axis stage. The probe was inserted from the rear side of the cylindrical anode as shown in Fig. 2, and was evacuated behind a shield placed aside to avoid severe contamination of the probe. The insulating tube made of alumina was 4 mm in diameter and wrapped a tungsten wire of 0.3 mm in diameter pushed out by 0.5 mm in length. The measuring points ranged along the centerline, and the probe was also traversed in the radial direction at 10 mm and 18 mm apart from the cathode end as shown in Fig. 2. The probe was kept about 1 second at the measured points, and then bias voltage with a triangular wave of -35 V to 35 V was applied to the probe at 1.5 Hz.

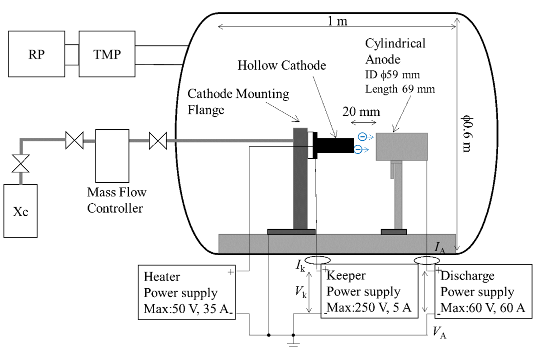

Figure 1. Vacuum chamber.

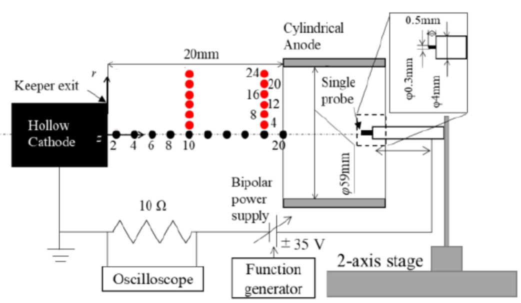

Figure 2. Prove measurement system.

C. Working Condition

The discharge mode focused on in this paper is the spot mode known as a static condition with minute oscillation of discharge properties, because the spot mode is the ideal condition to use in the actual operation in space. One of the working conditions of the spot mode observed for the laboratory model is shown in Table 1. Since the transition from plume to spot mode occurred between 20 and 30 sccm, the condition with a mass flow rate of 40 sccm was quite stable. The experiment was conducted under the constant current condition, and then the resultant discharge (anode) voltage and keeper voltage were 14 and 13 V, respectively. To consider the background pressure, when the neutral pressure becomes lower than the specified value obtained in the experiment, macroneutrals were supplemented to maintain the minimum pressure.

III. Numerical Modeling

A. Hybrid-PIC Model

Table 1. **Working condition.**

Gas	Xenon
Mass flow rate	40 sccm
Discharge current	20 A
Keeper current	3.0 A
Background pressure	4.8 $\times 10^{-2}$ Pa

As a numerical model of hollow cathodes, fluid models have been studied for years due to its high capability to treat high-density plasma inside the cathode. In this study, we have been developing a hybrid-PIC code, in which heavy species (neutrals and ions) and electrons are modeled as particles and fluid, respectively. The hybrid-PIC model enables simulation including widely ranging density from inside to outside the cathode with a single physical model, and it can handle arbitrary ion energy distribution which will strongly affect the sputtering rate on the walls.[10,14] In the model, we assume that the flow is axisymmetric and quasi-neutral in the computational domain, therefore thin sheath approximation is imposed on the wall boundaries. The trajectories of ions are traced with PIC method, where the elastic collisions (n-n, n-i, i-i) and the charge exchange collision (CEX) are taken into account. The collisions with regard to neutrals are dealt with DSMC (Direct Simulation Monte Carlo) method, and the Coulomb collision between ions is dealt with MCC (Monte Carlo Collision) method to reduce the computational cost. In the CEX model, the effect of the polarization potential which can lead to a large scattering angle is considered via Nanbu's model.[15] The nominal weight of a macroneutral was set much larger than that of a macroion to reduce the computational cost, thus a mass decay model was employed as an ionization model.[16]

As mentioned above, the numerical model was updated so that the induced magnetic field could be considered. In the drift-diffusion model, the electron's velocity with the azimuthal induced magnetic field is given by

$$\boldsymbol{u}_e = \begin{pmatrix} u_{e,r} \\ u_{e,z} \end{pmatrix} = -\bar{\mu}\boldsymbol{E} - \frac{\bar{\mu}}{en_e}\nabla p_e, \quad \bar{\mu} = \mu_{e,\perp}\begin{pmatrix} 1 & \beta_e b_\theta \\ -\beta_e b_\theta & 1 \end{pmatrix} \tag{1}$$

$$b_\theta = \frac{B_\theta}{|\boldsymbol{B}|}, \quad \mu_{e,\perp} = \frac{\mu_{e,\parallel}}{1+\beta_e^2}, \quad \mu_{e,\parallel} = \frac{e}{m_e(\nu_{eh}+\nu_a)}, \quad \beta_e = \frac{e|\boldsymbol{B}|}{m_e(\nu_{eh}+\nu_a)}$$

where it is assumed that no external magnetic field is applied in the axial and radial directions. Because of this and axisymmetric assumptions, the azimuthal component of the electron velocity can be vanished regardless of the presence of the induced magnetic field. The magnetic flux density induced in the azimuthal direction is determined by,

$$B_\theta(z,r) = \frac{\mu_0}{2\pi r}\int_{S_r} \boldsymbol{j}(z,r)\cdot d\boldsymbol{S} \tag{2}$$

where S_r denotes the area inside the circle with the radius r. It is not necessary to consider the other components of the induced field due to the assumptions of axisymmetry and no external magnetic field.

With Eq.(1), the current conservation law is reduced to the elliptic equation with regard to the electric potential.

$$\nabla\cdot n_e\bar{\mu}\nabla\phi = \nabla\cdot n_e\left(\boldsymbol{u}_i + \frac{\bar{\mu}}{en_e}\nabla p_e\right) \tag{3}$$

The steady-state electron's energy conservation law is given by,[17]

$$\nabla\cdot\left(\frac{5}{2}n_e kT_e\boldsymbol{u}_e - \frac{5n_e k^2 T_e}{2e}\bar{\mu}\nabla T_e\right) = \boldsymbol{j}_e\cdot\boldsymbol{E} - \sum_{s=n,i} 3n_e k\frac{m_e}{m_i}\nu_{es}(T_e - T_s) - eV_{iz}k_{iz}n_n n_e + Q_{IAT}, \tag{4}$$

where V_{iz} and k_{iz} are the ionization energy and the forward reaction rate of ionization, respectively.[18] The last term in the right hand side is described in the next section.

The heavy particle's temperatures were evaluated as,[19]

$$T_s = \frac{m_s}{3k}\left(\langle v_s^2\rangle - \langle v_s\rangle^2\right), \quad s = n, i \tag{5}$$

where $\langle x\rangle$ denotes the average of x within a cell. Equations (3) and (4) were discretized using the Galerkin finite element method, and the electric potential and electron temperature were separately determined by solving these equations using a direct solver.[20]

B. IAT Growth Model

In the evaluation of the mobility and Hall parameter, the anomalous collision frequency ν_a associated with IAT is also included, where the frequency ν_a was determined by solving the time developing equation of the wave growth model,[9–11]

$$\frac{\partial W_T}{\partial t} + \nabla \cdot [(c_s \hat{\boldsymbol{u}}_d + \boldsymbol{u}_i) W_T] = 2\gamma W_T, \tag{6}$$

where

$$c_s = \sqrt{\frac{kT_e}{m_i}}, \quad \hat{\boldsymbol{u}}_d = \frac{\boldsymbol{u}_d}{|\boldsymbol{u}_d|}, \quad \boldsymbol{u}_d = \boldsymbol{u}_e - \boldsymbol{u}_i, \tag{7}$$

$$\gamma = \sqrt{\frac{\pi}{8}}\omega_0 \left[\left(\frac{m_e}{m_i}\right)^{1/2} \left(\frac{|\boldsymbol{u}_d|}{c_s} - 1\right) - \left(\frac{T_e}{T_i}\right)^{3/2} \exp\left(-\frac{T_e}{2T_i}\right) \right] - \frac{\nu_{in}}{2}. \tag{8}$$

Here ω_0 is a constant standing for the cutoff frequency of the instability. The anomalous collision frequency ν_a is given by,

$$\nu_a = \alpha \omega_{pe} \frac{W_T}{n_e k T_e}, \tag{9}$$

where α is a constant of $O(10^{-2})$. In this study, the upper and lower limits of the wave energy density were set as follows.

$$W_{T,max} = \frac{\nu_{st} n_e k T_e}{\alpha \omega_{pe}}, \quad W_{T,min} = 10^{-4} W_{T,max} \tag{10}$$

where ν_{st} represents the anomalous collision frequency for saturated state suggested by Sagdeev.

$$\nu_{st} = \alpha_{st} \omega_{pi} \frac{|\boldsymbol{u}_d|}{c_s} \tag{11}$$

Here the effect of the ratio T_e/T_i is confined to α_{st} following preceding studies.[21,22] According to Ortega et al.,[11] the order of magnitude of this parameter is 10^{-2}. The last term in the right hand side of Eq. (4) is attributed to the cooling of the electrons due to the IAT.[9,10]

$$Q_{IAT} = -\frac{\alpha}{2} \omega_{pi} W_T \left[\left(\frac{m_e}{m_i}\right)^{1/2} \left(\frac{|\boldsymbol{u}_d|}{c_s} - 1\right) + \left(\frac{T_e}{T_i}\right)^{3/2} \exp\left(-\frac{T_e}{2T_i}\right) \right] \tag{12}$$

The ion heating effect was ignored in this paper because the mass flow rate used in the working condition in Table 1 was so high that severe instability associated with IAT was not expected.

C. Calculation Conditions

The boundary conditions are summarized in Fig. 3. The computational domain in the plume region was truncated in front of the anode, and the electric potential and electron temperature were fixed to specified values based on the probe measurements along the truncated boundary because the discharge observed in the experiment was quite quiescent. Based on the experimental data, the specified electron temperature was linearly changed in the radial direction to consider the radial variation, but the electric potential was fixed to a constant value along the truncated rightmost boundary. Along the upper boundary in the plume region, the net current was set to zero, and the electron temperature was fixed. The specific values at these boundaries are tabulated in

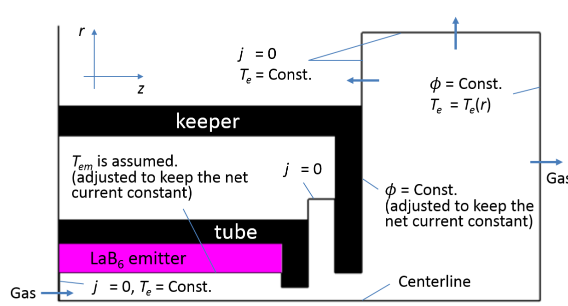

Figure 3. Boundary conditions.

Table 2. **Input parameters.**

Potential at right boundary	14 V
Electron temp. at right plume boundary (linearly varied outward)	1.2 - 0.75 eV
Electron temp. at upper plume boundary	0.75 eV
Electron temp. at inlet	0.8 eV
ω_0 in Eq. (8)	10^5 s^{-1}
α in Eq. (9)	10^{-2}
α_{st} in Eq. (11)	2.5×10^{-2}

Table 2. Thin sheath approximation was assumed on the whole wall surfaces, and the sheath model was imposed on the boundaries, which prescribes electron flux flowing into the walls.[14] On the emitter surface, the thermionic current was also taken into account with Richardson-Dushman formula including Schottky effect. When the sheath voltage becomes relatively low, however, space charge limitation might occur locally on the emitter surface. Therefore, a space charge limited current was locally evaluated and was set as a maximum value of the thermionic current. On the keeper surface, keeper current was calculated from the electron and ion fluxes, and the keeper voltage was periodically adjusted to maintain the keeper current constant. On the emitter surface, the emitter temperature distribution should be given to evaluate the thermionic electron current using Richardson-Dushman formula. In this study, a quadratic function in the following form was assumed as an emitter temperature distribution,

$$T_{em}(\hat{z}) = a_{em}(\hat{z} - \hat{z}_0)^2 + T_{em,0}, \quad \hat{z} = \frac{z}{L_{em}} \tag{13}$$

where L_{em} is the length of the emitter. The emitter temperature was assumed to reach a maximum value $T_{em,0}$ at $z = z_0$. In this paper, $\hat{z}_0 = 0.9$ was assumed, and the coefficient a_{em} was set so that $T_{em}(0)/T_{em,0} = 0.7$. The maximum temperature of $T_{em,0}$ was periodically adjusted to keep the discharge current close to a specified value.

The IAT growth model used here contains an unknown parameter of cutoff frequency ω_0 which prescribes the lower limit of the frequency IAT occurs. This parameter was introduced based on the empirical evidence that such a lower limit exists, and has been parameterized in the previous studies. In this study, we set a typical value of $\omega_0 = 10^5 s^{-1}$, although we have not measured the spectra of IAT.

IV. Results and Discussion

A. Comparison between Simulation and Experiment

To validate the simulation results, the axial and radial plasma properties such as electron number density, electric potential, and electron temperature are compared in Figs. 4 and 5, respectively. The black and red lines show the simulated results without and with the induced magnetic field, respectively.

In Fig. 4, the horizontal axis is the axial distance from the exit of the keeper electrode normalized by the emitter length. We can see that the measured electron number density was monotonically decreased but was kept about 10^{18} m^{-3} around z_k/L_{em}=0.7, while the simulation result without the magnetic field reaches 10^{17} m^{-3} at the same location. However, this discrepancy is considerably improved by considering the magnetic field, while there is still slight underestimation over all measured points. Since each experimental plot was obtained by a single-shot probe insertion, we evaluated the error bar for the electron number density from the fluctuation of the probe current around the space potential. As a result, the order of magnitude of the errors for all plots are estimated as less than 10^{17} m^{-3}, therefore we can not depict discernible error bars. The reason for the discrepancy might be the blockage effect caused by the probe with a diameter of 4 mm. This speculation is bolstered by the fact that the discrepancy is gradually diminished with distance from the cathode end. Of course, since further tuning of the model parameters might improve the accuracy, investigation with a wide range of parameters is necessary in the future. As for the electric potential, the experimental data show a moderate decrease along the center axis, but the result without the magnetic field is slightly overestimated near the cathode and show steeper decay. On the other hand, with the magnetic field, the profile gets flattened and is slightly underestimated compared with the experimental data, which

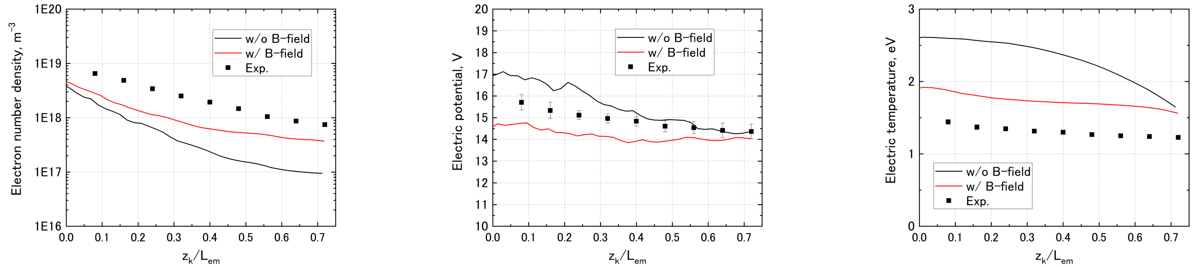

(a) Electron number density. (b) Electric potential. (c) Electron temperature.

Figure 4. Axial profiles of plasma properties along the center axis for $\dot{m}$ = 40 sccm, I_d = 20 A, I_k = 3.0 A. The black and red lines show the simulated results without and with the induced magnetic field, respectively. z_k is the axial distance from the cathode end.

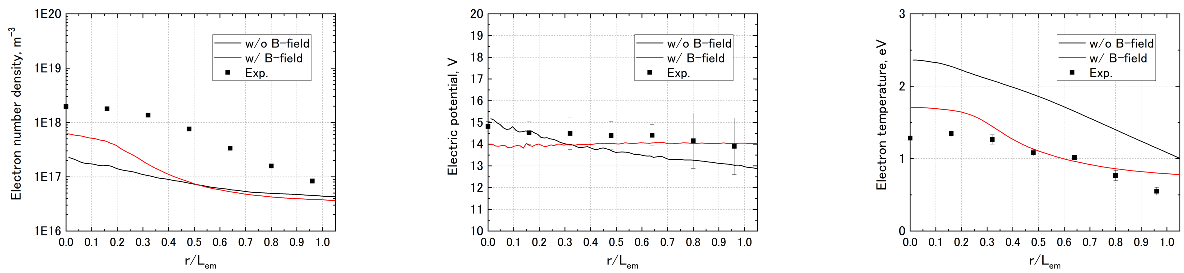

(a) Electron number density. (b) Electric potential. (c) Electron temperature.

Figure 5. Radial profiles of plasma properties at 10 mm from cathode end for $\dot{m}$ = 40 sccm, I_d = 20 A, I_k = 3.0 A. The black and red lines show the simulated results without and with the induced magnetic field, respectively.

suggests that the axial profile of the electric potential is relatively insensitive to the magnetic field. We can see the electron temperature is considerably decreased and approaches the experimental data when including the magnetic field, which would be attributed to the increase in the electron number density as mentioned above. Although The electron temperature is still overestimated about 0.4 eV, parameter survey for the present model might improve these differences

Figure 5 shows the radial profiles of plasma properties at 10 mm apart from the cathode end. As a whole, we can see that quantitative accuracy is improved by including the induced magnetic field. The potential profile is flattened by the effect of the magnetic field, and agree well with the experimental data. The electron temperature is decreased and approaches the experimental data, whereas the shape of the profile is slightly different. In addition, the profile of the electron number density exhibits qualitative discrepancy. This discrepancy might be attributed to a disregard of the existence of the anode which would reflect some particles toward the cathode.

B. Flow Field Structure

The improvement of the accuracy along the center axis by including the magnetic field should be understood in terms of the flow field structure. To this end, the numerical density, electric potential, and electron temperature distributions are shown in Fig. 6. The left and right columns correspond to the results without and with the induced magnetic field, respectively.

Without the magnetic field, the electron number density inside the cathode tends to diffuse up to the inlet, namely, the entrance of the emitter region, while its order of magnitude at the inlet for the case with the magnetic field is still 10^{17} m^{-3} as seen in Fig. 6(b). We infer that this low electron number density near the inlet is attributed to the low electron temperature in this region as shown in Fig. 6(f). The low electron temperature leads to not only a slow ionization process but also low sheath potential on the emitter

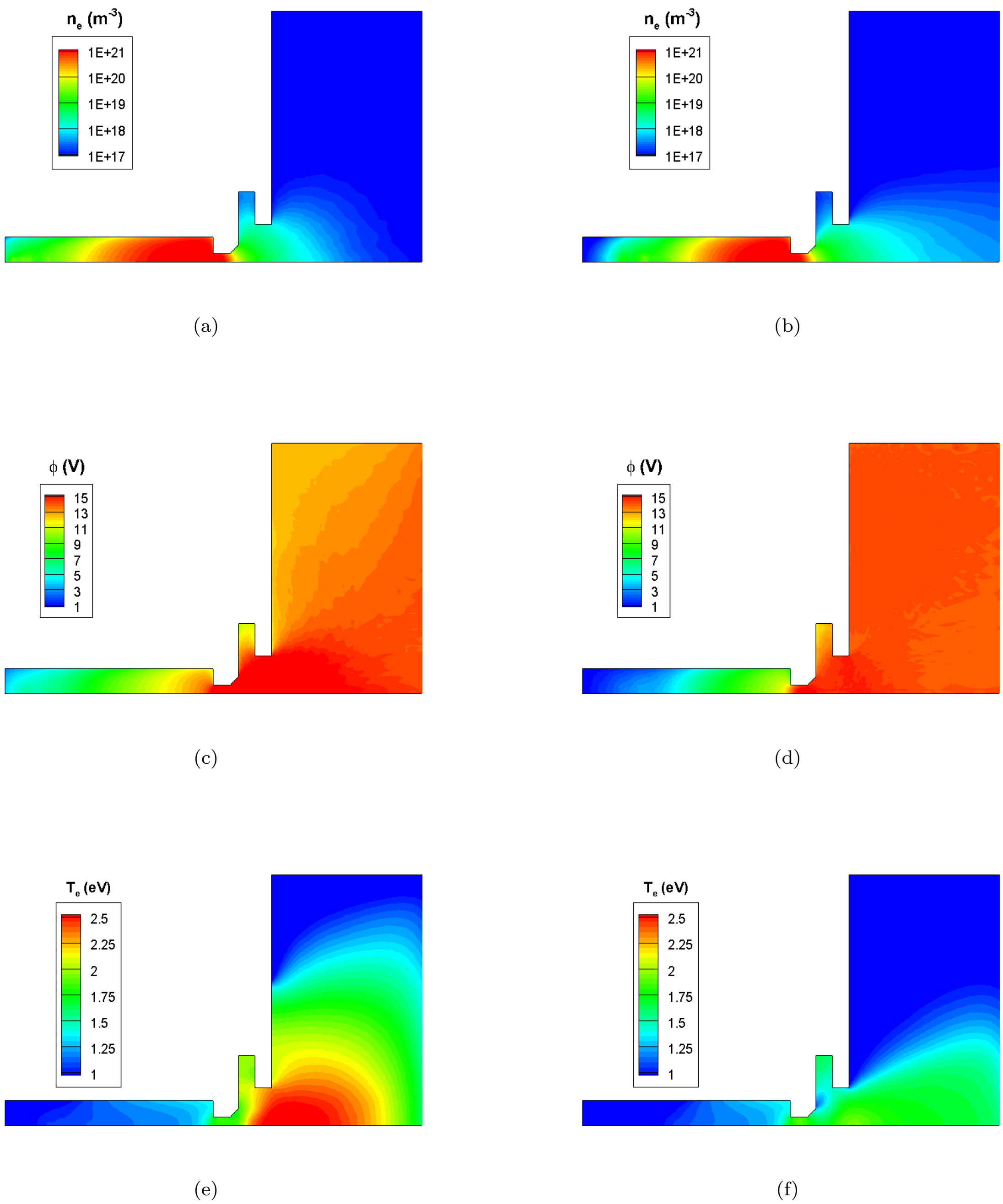

Figure 6. Plasma flows for $\dot{m}$ = 40 sccm, I_d = 20 A, I_k = 3.0 A, $\omega_0 = 10^5$ s^{-1} (top: electron number density, middle: electric potential, bottom: electron temperature). The left and right columns correspond to the results without and with the induced magnetic field in the azimuthal direction, respectively.

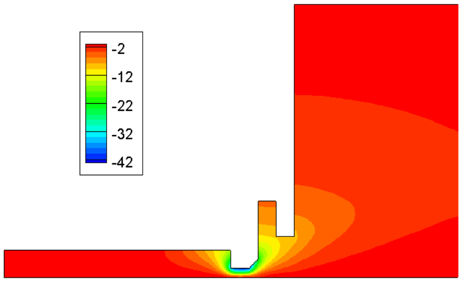

Figure 7. Induced magnetic flux density for $\dot{m} = 40$ sccm, $I_d = 20$ A, $I_k = 3.0$ A, $\omega_0 = 10^5$ s^{-1}, Gauss.

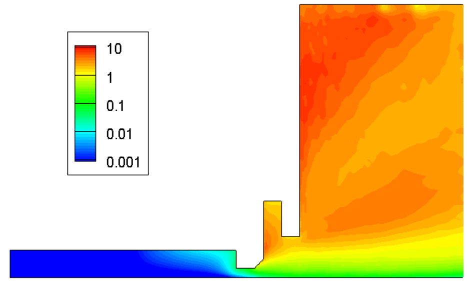

Figure 8. Electron's Hall parameter for $\dot{m} = 40$ sccm, $I_d = 20$ A, $I_k = 3.0$ A, $\omega_0 = 10^5$ s^{-1}.

surface, which gives rise to a large amount of electron loss through the ion-repelling sheath. Since the low sheath potential on the emitter surface also promotes the decrease in the electron energy, namely electron temperature, this spiral results in such a low potential and low-temperature distribution. The low sheath potential is also associated with the low space potential near the inlet as seen in Fig. 6(d), because high space potential is a necessary condition to maintain high sheath potential on the wall. The low space potential near the inlet is attributed to the enhanced resistivity due to the induced magnetic field in the azimuthal direction. Figures 7 and 8 show the distributions of the induced magnetic flux density and electron's Hall parameter, respectively. The magnitude of magnetic flux density is highest inside the orifice due to constriction of the discharge current, while Hall parameter grows through the orifice region and reaches a maximum in the plume region because of a rapid decrease in the collision rate. From the orifice to the plume region, the Hall parameter ranges from 0.1 to 10, which serves to enhance the resistivity in z-r plane. Since the space potential is fixed at the end of the plume region, the high resistivity from the orifice to the plume region results in low space potential inside the cathode.

With the magnetic field, the electron number density in the plume region tends to be constricted toward the center axis, which directly leads to the improvement of the accuracy along the center axis mentioned earlier. This is attributed to the pinch effect caused by Lorentz force $\boldsymbol{j} \times \boldsymbol{B}$ acting on the plasma. We can also see that the radial profile of the electric potential is flattened over the plume region by including the magnetic field as seen in Fig. 5(b). This tendency can be understood as follows. According to the equation of motion for electrons, the gradient of the electric potential is given by,

$$\nabla \phi = \frac{\nabla p_e}{e n_e} + \boldsymbol{u}_e \times \boldsymbol{B} + \frac{\boldsymbol{u}_e}{\mu_e}. \tag{14}$$

The effect of the magnetic field is described as the second term in the right hand side. The radial component of the term $\boldsymbol{u}_e \times \boldsymbol{B}$ is basically positive in the plume region, therefore this term serves to increase $(\nabla \phi)_r$. Consequently, the potential profile gets flattened by the effect of $\boldsymbol{u}_e \times \boldsymbol{B}$.

V. Conclusion

The results of hybrid-PIC simulation of a hollow cathode were compared with the experimental data of probe diagnosis in the plume region. The numerical model treats the heavy species (neutrals and ions) and electrons as particles and fluid, respectively, and was updated so that the induced magnetic field in the azimuthal direction can be considered. The growth of ion acoustic turbulence (IAT) was taken into account by solving the time-developing equation of the ion acoustic wave, which enables us not to assume a saturated state of the instability.

In this paper, we focused on spot mode which is thought an ideal operating mode of a hollow cathode and performed simulations with and without the induced magnetic field. In the experiment, a Langmuir probe was inserted from the rear side of the cylindrical anode along the center axis to measure electron number density, electric potential, and electron temperature. The results show that the electron number density was underestimated when the induced magnetic field was ignored, but the discrepancy can be considerably improved by including the induced magnetic field due to the pinch effect, while there are still quantitative differences within several tens of percents. The induced magnetic field serves to flatten the axial and radial profiles of electric potential and to decrease electron temperature over the plume region. However, the present model is inadequate to capture the radial profile, especially of the electron number density, therefore further investigation is necessary in the future. It was also shown that the effect of the induced magnetic field enhances the electrical resistivity, especially from the orifice to the plume region, where the Hall parameter ranges from 0.1 to 10. Consequently, the space potential inside the cathode is decreased, and electron number density and electron temperature are also reduced especially near the upstream side of the emitter.

Acknowledgments

This research has been supported by JSPS KAKENHI Grant Number 17H01353.

References

[1]Lev, D., Myers, R. M., Lemmer, K. M., Kolbeck, J., Koizumi, H., and Polzin, K., "The technological and commercial expansion of electric propulsion," *Acta Astronautica*, Vol. 159, 2019, pp. 213–227.

[2]Hoskins, W. A., Cassady, R. J., Morgan, O., Myers, R. M., Wilson, F., King, D. Q., and deGrys, K., "30 Years of Electric Propulsion Flight Experience at Aerojet Rocketdyne," *33rd International Electric Propulsion Conference*, IEPC-2013-439, 2013.

[3]Vial, V., Cornu, N., Coulaud, E., and Arrat, D., "PPS®NG: Hall Effect thruster for next generation," *32nd International Electric Propulsion Conference*, IEPC-2011-120, 2011.

[4]Duchemin, O., Méhauté, D. L., Öberg, M., Cavelan, X., Guilhem-Ducléon, M., Khimeche, G., Payot, F., Soubrier, L., Galiana, D., and Glorieux, G., "End-to-End Testing of the PPS®5000 Hall Thruster System With a 5-kW Power Processing Unit," *34th International Electric Propulsion Conference*, IEPC-2015-127, 2015.

[5]Hofer, R. R., Polk, J. E., Sekerak, M. J., Mikellides, I. G., Kamhawi, H., Sarver-Verhey, T. R., Herman, D. A., and Williams, G., "The 12.5 kW Hall Effect Rocket with Magnetic Shielding (HERMeS) for the Asteroid Redirect Robotic Mission," *52nd AIAA/SAE/ASEE Joint Propulsion Conference*, AIAA-2016-4825, 2016.

[6]Hamada, Y., Bak, J., Kawashima, R., Koizumi, H., Komurasaki, K., Yamamoto, N., Egawa, Y., Funaki, I., Iihara, S., Cho, S., Kubota, K., Watanabe, H., Fuchigami, K., Tashiro, Y., Takahata, Y., Kakuma, T., Furukubo, Y., and Tahara, H., "Hall Thruster Development for Japanese Space Propulsion Programs," *Trans. Japan Soc. Aero. Space Sci.*, Vol. 60, No. 5, 2017, pp. 320–326.

[7]Yamamoto, N., Takase, K., Hirano, Y., Komurasaki, K., Kakami, A., Tsukizaki, R., Hosoda, S., Kuninaka, H., and Yokota, S., "Thrust Performance in a 5 kW Class Anode Layer Type Hall Thruster," *Trans. Japan Soc. Aero. Space Sci., Aerospace Technology Japan*, Vol. 14, No. ists30, 2016, pp. Pb_183–Pb_187.

[8]Funaki, I., Cho, S., Sano, T., Fukatsu, T., Tashiro, Y., Shiiki, T., Nakamura, Y., Watanabe, H., Kubota, K., Matsunaga, Y., and Fuchigami, K., "1,000-hours Demonstration of a 6-kW-class Hall Thruster for All-Electric Propulsion Satellite," *Trans. Japan Soc. Aero. Space Sci., Aerospace Technology Japan*, Vol. 17, No. 5, 2019, pp. 589–595.

[9]Jorns, B. A., Ortega, A. L., and Mikellides, I., "First-principles Modeling of the IAT-driven Anomalous Resistivity in Hollow Cathode Discharges I: Theory," *52nd AIAA/SAE/ASEE Joint Propulsion Conference*, AIAA-2016-4626, 2016.

[10]Kubota, K., Oshio, Y., Watanabe, H., Cho, S., and Funaki, I., "Numerical Simulation of Hollow Cathode with Hybrid-PIC Coupled with Growth Model of Ion Acoustic Turbulence," *2018 Joint Propulsion Conference*, AIAA-2018-4513, 2018.

[11]Ortega, A. L., Jorns, B. A., and Mikellides, I. G., "Hollow Cathode Simulations with a First-Principles Model of Ion-Acoustic Anomalous Resistivity," *Journal of Propulsion and Power*, Vol. 34, No. 4, 2018, pp. 1026–1038.

[12]Kubota, K., Oshio, Y., Watanabe, H., Cho, S., Ohkawa, Y., and Funaki, I., "Numerical and Experimental Study on Discharge Characteristics of High-Current Hollow Cathode," *52nd AIAA/SAE/ASEE Joint Propulsion Conference*, AIAA-2016-4628, 2016.

[13]Goebel, D. M., Watkins, R. M., and Jameson, K. K., "LaB6 Hollow Cathodes for Ion and Hall Thrusters," *Journal of Propulsion and Power*, Vol. 23, No. 3, 2007, pp. 552–558.

[14]Kubota, K., Oshio, Y., Watanabe, H., Cho, S., Ohkawa, Y., and Funaki, I., "Hybrid-PIC Simulation of LaB6 Hollow Cathode Self-Heating Characteristics," *Trans. Japan Soc. Aero. Space Sci.*, Vol. 62, No. 1, 2019, pp. 11–19.

[15]Nanbu, K., "Probability Theory of Electron-Molecule, Ion-Molecule, Molecule-Molecule, and Coulomb Collisions for Particle Modeling of Materials Processing Plasmas and Gases," *IEEE Transactions on Plasma Science*, Vol. 28, No. 3, 2000, pp. 971–990.

[16]Parra, F. I., Ahedo, E., Fife, J. M., and Martinez-Sanchez, M., "A two-dimensional hybrid model of the Hall thruster discharge," *Journal of Applied Physics*, Vol. 100, No. 2, 2006, pp. 023304.

[17]Sutton, G. W. and Sherman, A., *Engineeriing Magnetohydrodynamics*, Dover Publications, Inc., New York, 2006.

[18]Goebel, D. M. and Katz, I., *Fundamentals of Electric Propulsion: Ion and Hall Thrusters*, JOHN WILEY & SONS, INC., 2008.

[19]Bird, G. A., *Molecular Gas Dynamics and the Direct Simulation of Gas Flows*, OXFORD, 1994.

[20]Amestoy, P. R., Duff, I. S., L'Excellent, J.-Y., and Koster, J., "A fully asynchronous multifrontal solver using istributed dynamic scheduling," *SIAM Journal of Matrix Analysis and Applications*, Vol. 23, No. 1, 2001, pp. 15–41.

[21]Mikellides, I. G., Guerrero, P., Ortega, A. L., Goebel, D. M., and Polk, J. E., "Investigations of Spot-to-plume Mode Transition in a Hollow Cathode Discharge Using 2-D Axisymmetric Plasma Simulations," *2018 Joint Propulsion Conference*, AIAA 2018-4722, 2018.

[22]Mikellides, I. G., Goebel, D. M., Jorns, B. A., Polk, J. E., and Guerrero, P., "Numerical Simulations of the Partially-ionized Gas in a 100-A LaB6 Hollow Cathode," *33rd International Electric Propulsion Conference*, IEPC-2013-142, 2013.